Accepted Manuscript

The ion-irradiation tolerance of the pyrochlore to fluorite $Ho_{(x)}Yb_{(2-x)}TiO_5$ and Er_2TiO_5 compounds: A TEM comparative study using both *in-situ* and bulk *ex-situ* irradiation approaches

Robert D. Aughterson, Gregory R. Lumpkin, Katherine L. Smith, Massey de los Reyes, Joel Davis, Maxim Avdeev, Mark C. Ridgway, Julie M. Cairney

PII: S0022-3115(17)31834-2

DOI: 10.1016/j.jnucmat.2018.05.026

Reference: NUMA 50955

To appear in: *Journal of Nuclear Materials*

Received Date: 27 December 2017

Revised Date: 11 April 2018

Accepted Date: 8 May 2018

Please cite this article as: R.D. Aughterson, G.R. Lumpkin, K.L. Smith, M.d.l. Reyes, J. Davis, M. Avdeev, M.C. Ridgway, J.M. Cairney, The ion-irradiation tolerance of the pyrochlore to fluorite $Ho_{(x)}Yb_{(2-x)}TiO_5$ and Er_2TiO_5 compounds: A TEM comparative study using both *in-situ* and bulk *ex-situ* irradiation approaches, *Journal of Nuclear Materials* (2018), doi: 10.1016/j.jnucmat.2018.05.026.

The ion-irradiation tolerance of the pyrochlore to fluorite $Ho_{(x)}Yb_{(2-x)}TiO_5$ and Er_2TiO_5 compounds: a TEM comparative study using both *in-situ* and bulk *ex-situ* irradiation approaches.

Robert D. Aughterson [a, c, *], Gregory R. Lumpkin [a], Katherine L. Smith [a], Massey de los Reyes [a], Joel Davis [a], Maxim Avdeev [a], Mark C. Ridgway [b], Julie M. Cairney [c]

[a] Australian Nuclear Science and Technology Organisation, Lucas Heights, NSW 2234, Australia

[b] Centre for Science and Engineering of Materials, Australian National University, Canberra, ACT 0200, Australia

[c] Australian Centre for Microscopy and Microanalysis, The University of Sydney, NSW 2006, Australia

*Corresponding author: Robert D. Aughterson,

Email: roa@ansto.gov.au , Phone: +61 29717 3600

Gregory Lumpkin: gregory.lumpkin@ansto.gov.au
Katherine Smith: kath.smith@dfat.gov.au
Massey de los Reyes: massey.delosreyes@sa.gov.au
Joel Davis: joel.davis@ansto.gov.au
Maxim Avdeev: maxim.avdeev@ansto.gov.au
Julie Cairney: julie.cairney@sydney.edu.au

Abstract

We refine the crystal structures of a systematic series of compounds with the general composition $Ho_{(x)}Yb_{(2-x)}TiO_5$ (x = 2, 1.6, 1.2, 1, 0.8, 0.4, 0) and Er_2TiO_5 and find a transition from defect-pyrochlore to defect-fluorite structure with increasing ytterbium content, decreasing lanthanide radius. Short-range structure modulations consisting of pyrochlore-like nano-domains are systematically characterised using transmission electron microscopy. We test the Kr^{2+} 1 MeV ion-irradiation response of Ho_2TiO_5, $HoYbTiO_5$, Yb_2TiO_5, and Er_2TiO_5, via the crystalline to amorphous transition observed by using the *in-situ* TEM approach. The critical dose of amorphisation, D_c, was measured at various temperatures and used to calculate the critical temperature for maintaining crystallinity, T_c. A trend of lower T_c values with decreasing lanthanide radius is found. We describe a new approach for determining T_c values using cross-sectional TEM analysis of *ex-situ* bulk irradiated, 1 MeV Se^+, samples; Ho_2TiO_5, $HoYbTiO_5$ and Yb_2TiO_5. The results of D_c and T_c values using the two approaches vary; however the trends across the sample system remain the same.

Keywords: In-situ transmission electron microscopy; Ion irradiation; Ceramics; Crystallography; Ln_2TiO_5

1. Introduction

For designer ceramic materials the inherent property of resistance to amorphisation upon exposure to high energy particles is desirable in materials used within nuclear applications. These applications include damage resistant cladding and coatings, inert matrix fuels, waste-forms or structural materials. The Ln_2TiO_5 (Ln = lanthanides and yttrium) compounds are technologically interesting because they are found as burnable poisons within some nuclear fuels [1,2], and occur in prototype nuclear waste forms [3-6,7].

For candidate nuclear waste-form materials to be successful they should be capable of incorporating a large range of radio-isotopes, chemically durable, and radiation tolerant. In this study we focus on the ion-irradiation response of a system of ceramic oxides with the Ln_2TiO_5 stoichiometry. Previously, fundamental ion-irradiation studies, using *in-situ* ion-irradiation with TEM characterisation, have looked at the radiation response of several compounds within the Ln_2TiO_5 series[5,6,7,8]. These studies showed a trend toward improved radiation response, i.e. a lowering of the critical temperature above which the specimen remains crystalline, for those lanthanide titanates that had either cubic symmetry or were more energetically likely to transition to cubic symmetry.

Some isotopes of dysprosium and gadolinium have relatively large thermal neutron cross-sections and so have been considered for use as burnable poisons. Gd_2TiO_5 has been studied as a potential phase within the nuclear fuel matrix [2]. The thermo-physical properties of both Gd_2TiO_5 and Dy_2TiO_5 have been studied to test their suitability for use as burnable poisons within

the nuclear reactor environment [9]. The compound Dy_2TiO_5 has been used as part of the control rod material within Russian Water-Water Energetic Reactor (WWER) type reactors [10]. Of the three polymorphs of Dy_2TiO_5 discussed the defect-fluorite structure was found to have the least amount of swelling upon exposure to irradiation.

According to the temperature stability diagram proposed by Shepelev and Petrova [11], lanthanide titanates of nominal stoichiometry Ln_2TiO_5 can take on cubic symmetry, if heated to high enough sintering temperature, when the lanthanide is of terbium ionic radius size or smaller (i.e. Ln = Tb, Dy, Ho, Er, Tm, Yb and Lu). The cubic series of Ln_2TiO_5 compounds have also been studied as part of a broader study of the $Ln_2(Ti_{2-x}Ln_x)O_{7-x/2}$ solid solutions [12]. These solid solutions spanned between end members $Ln_2Ti_2O_7$, an ideal pyrochlore, to Ln_2TiO_5, characterised as a defect-pyrochlore. The solid solution study showed compounds with Ln_2TiO_5 stoichiometry and defect-pyrochlore structure had a sequentially-decreasing cell length for compounds from Tb_2TiO_5 to Lu_2TiO_5.

In a neutron diffraction study by Lau *et al*. Ho_2TiO_5 and Yb_2TiO_5 compounds were investigated [13]. The structures were refined using the pyrochlore symmetry, *Fd*$\bar{3}$*m*, which gave cell parameters of 10.3027 (2) and 10.1857 (1) Å for Ho_2TiO_5 and Yb_2TiO_5 respectively. The pyrochlore structure can be considered a 2 x 2 x 2 super-cell of the fluorite structure with ordering of the A and B cation sites in pyrochlore whilst the cation site occupancies are randomised in fluorite. Whilst the structures were refined using the pyrochlore symmetry it was noted that these materials actually consisted of long-range defect-fluorite and short-range defect-pyrochlore structures. It has also been

shown that Ho_2TiO_5 will form different sized domains of pyrochlore symmetry depending on the heating and cooling regime used during sintering[14]. This same effect, using either rapid or slow cooling, has been observed for the Yb_2TiO_5, Tm_2TiO_5 and Er_2TiO_5 compounds[15].

Aughterson and co-workers have previously published crystal structure data for the Yb_2TiO_5 compound with the symmetry being described as long range defect-fluorite ($Fm\bar{3}m$) a = 5.09418 (9) Å, with short range, nano-domain, defect-pyrochlore ($Fd\bar{3}m$) symmetry. This was based on neutron diffraction data and transmission electron microscope (TEM) selected area diffraction patterns and bright field images [16]. This is in agreement with the findings by Lau *et al*. for the Yb_2TiO_5 compound [13]. The refined cell parameters for Yb_2TiO_5 from the two studies match well, allowing for the difference in space group used in the refinements.

In a separate study it was also shown that by using different ratios of lanthanides samarium and ytterbium ($Sm_{(x)}Yb_{(2-x)}TiO_5$, where x = 2, 1.4, 1, 0.6 and 0) it is possible to fabricate samples with the four main crystal structures of the Ln_2TiO_5 series. Both $Sm_{0.6}Yb_{1.4}TiO_5$ and Yb_2TiO_5 were found to have long range defect-fluorite and short range defect-pyrochlore structures but the former compound had the larger pyrochlore domains of these two [16].

There has been considerable work, both experimental and modelling, on the radiation response of the $Ln_2Ti_2O_7$ pyrochlore series [17,18,19]. The observed trend of improvement in radiation tolerance with decreasing lanthanide size, from gadolinium to lutetium, is attributed to the more energetically favourable transition to defect-fluorite structure upon exposure to ion-irradiation for the smaller lanthanide compounds[17]. The smaller lanthanides, due to their size

tending toward that of titanium will have greater thermodynamic stability toward Ln-Ti anti-site disordering, leading to formation of the defect-fluorite structure.

In a study by Whittle *et al*., x-ray diffraction data revealed that the structure of the Y_2TiO_5, $YYbTiO_5$ and Yb_2TiO_5 series tended from defect-pyrochlore to defect-fluorite with the introduction of ytterbium [7]. There was a corresponding improvement in radiation response, i.e. a lowering of critical temperature of crystallinity (T_c), with increasing ytterbium content, which was related to the greater disordering associated with the increasing presence of defect-fluorite structure. This correlation between defect-fluorite and improved radiation response was further confirmed by comparing irradiation results with the pyrochlores $Y_2Ti_2O_7$ and $Yb_2Ti_2O_7$, which showed that the Y_2TiO_5 and Yb_2TiO_5 compounds perform better.

A previous, broader study looked at the four major Ln_2TiO_5 crystal structures and their radiation response[8]. The Sm_2TiO_5 (orthorhombic symmetry) and $SmYbTiO_5$ (hexagonal symmetry) compounds had relatively poor radiation tolerance, low critical dose of amorphisation and high critical temperature to maintain crystallinity. However, the $Sm_{0.6}Yb_{1.4}TiO_5$ and Yb_2TiO_5, both with cubic symmetry, showed a remarkable improvement in radiation tolerance.

All of the radiation response studies discussed here have utilised the TEM coupled with *in-situ* ion-irradiation approach. A review of this experimental approach and the facilities that support it is given by Hinks [20]. With TEM characterisation, there is a requirement that the specimen fragments used for analysis are thin enough to be electron transparent (~ 200 nm or less). This requirement has an effect of influencing radiation damage of the sample due

to the large surface area to volume ratio resulting in defects rapidly migrating to the surface[21]. If the critical dose of amorphisation is influenced by the thickness of the specimen the question then arises: do the *in-situ* experimentally determined critical temperature of crystallinity trends match those found for the bulk sample? There have been some studies comparing the TEM based *in-situ* results with bulk irradiation but none to date on the critical temperature trends [19,22,23]. Studies on bulk materials and their radiation response, relative to the thin wafers, will be more representative of the materials used for nuclear applications.

In this study we look at the *in-situ* ion-irradiation results of previously untested compounds Ho_2TiO_5, $HoYbTiO_5$, Er_2TiO_5, and previously tested Yb_2TiO_5, and compare these with other Ln_2TiO_5 systems of compounds and the related pyrochlore $A_2B_2O_7$ families of compounds. Previous studies have indicated a trend of sequential improvement in radiation response of cubic Ln_2TiO_5 compounds containing sequentially smaller lanthanides. This trend is tested in this study using both the systematic $Ho_{(x)}Yb_{(2-x)}TiO_5$ series and Er_2TiO_5, with the Er radius being close to that of the HoYb mixed lanthanide size. After establishing trends in radiation response, critical temperature of crystallinity, we seek to compare the results of our *in-situ* irradiation experiments with those found with *ex-situ* irradiated bulk samples characterised by using cross-sectional TEM. This is the first time *in-situ* and *ex-situ* TEM techniques for establishing the critical temperature of crystallinity have been directly compared.

2 Methods

2.1 Sample Preparation

Bulk, polycrystalline single phase materials were prepared by ball-milling stoichiometric amounts of Ho_2O_3, Yb_2O_3 and TiO_2 or Er_2O_3 (Ln_2O_3 sourced from Sky Spring Nanomaterials Inc., 99.9% purity) and TiO_2 (Aldrich, 99.9% purity). The mixed oxide powders were consolidated using a cold isostatic press operated at 400 MPa. The consolidated pellets were sintered to 1600 °C for 24 hours in air with a heating and cooling rate of 5 °C per minute.

2.2 SEM (EDX)

Scanning electron microscopy (SEM) was performed on a Zeiss Ultra Plus Gemini operated at 15 kV, which was equipped with an Oxford X-Max Silicon Drift Detector for energy dispersive x-ray analysis (EDX). The EDX data were collected and analysed using the Oxford INCA microanalysis software system.

2.3 Laboratory XRD

Powdered samples were analysed using x-ray diffraction carried out on a Panalytical X'pert Pro laboratory x-ray diffractometer with a weighted Cu Kα source, $K\alpha_1$ λ = 1.5405980 Å and $K\alpha_2$ λ = 1.5444260 Å. The diffractometer was operated in the Bragg reflection geometry with sample spinner on and diffraction data collected between 5 and 90 ° 2θ with a step size of 0.03 °. Rietveld structure analysis was carried out using the software Rietica [24].

2.4 Neutron Powder Diffraction

A powdered Ho_2TiO_5 sample loaded into a cylindrical vanadium container was analysed using neutron powder diffraction carried out on the Echidna powder diffraction beamline, Australian Nuclear Science and Technology Organisation

(ANSTO). Data was collected at ambient temperature using neutrons of wavelength 1.6215 Å.

2.5 Transmission Electron Microscopy (TEM)

TEM specimens for *in-situ* ion-irradiation were prepared by mortar and pestle of bulk samples into fine fragments (powder) and dispersed in ethanol. The ethanol powder mix was dispensed onto holey carbon film, supported by a copper grid, via pipette.

TEM specimen preparation of bulk irradiated samples was performed by first coating the sample surface with 3 nm of platinum in a Microvac MH7 Duo ion sputter coater. The TEM specimen preparation was carried out using a Zeiss Auriga 60 focused ion beam system using Kleindiek micromanipulator via a standard lift-out approach, with final milling conducted at progressively lower voltages (30, 15, 5 and 2kV) to minimise Ga damage.

TEM was carried out using a JEOL 2200FS operated at 200 kV and fitted with an Oxford X-Max 80 mm^2 energy dispersive x-ray spectroscopy (EDX) system. The EDX data was analysed using Oxford INCA, version 4.15, microanalysis software. Bright field images, selected area electron diffraction (SAED) and nano-beam electron diffraction (NBED) patterns were collected by using Gatan Orius and Ultrascan cameras.

2.6 In-situ ion-irradiation with TEM characterisation

TEM specimens, which took the form of finely ground crystal fragments on holey carbon film, were prepared as described in methods section 2.5.

The in-situ ion-irradiation coupled with TEM characterisation was carried out at the Argonne National Laboratory on a Hitachi H-9000-NAR TEM operated

at 300 kV, interfaced with an NEC ion accelerator. For a more detailed description of the facility the reader is referred to Kirk *et al*. [25].

Specimens were exposed to accelerated, 1 MeV Kr^{2+} ions, and monitored, *in-situ* using the TEM, for damage accumulation via collection of selected area diffraction patterns (SAED). Ion-irradiation and observation of the grains via the electron beam were carried out separately to prevent the dual beam synergistic effects on defect mobility. All specimens were subjected to a sufficient fluence to facilitate a crystalline to amorphous transition, with the final fluence termed critical dose of amorphisation and denoted D_c. The complete amorphisation was determined to be the point where no more crystalline reflections were observable within the SAED. Multiple measurements of D_c were carried out at temperatures between 50 and 700 K. The D_c versus temperature data was fit to the equation;

$$D_c = {D_0}\Big/{1 - \exp\left[\left(\frac{E_a}{k_B}\right)\left(\frac{1}{T_c} - \frac{1}{T}\right)\right]} \quad (1)$$

D_0 is the critical dose of amorphisation at 0 K, k_B is the Boltzmann constant and E_a is the activation energy for mobilisation of defects (equation taken from Weber [26]). The asymptote of this fit was used to calculate the critical temperature of crystallinity, T_c, the temperature above which the material maintains crystallinity regardless of the final fluence.

2.7 Heavy ion implantation

Previous to bulk sample ion-irradiation, samples of Ho_2TiO_5, $HoYbTiO_5$ and Yb_2TiO_5 had a surface polish to a 1 µm diamond suspension finish. Ion-irradiation was carried out using the tandem accelerator from the Department of Electronic Materials Engineering, Australian National University. The

specimens were exposed to 1 MeV Se^+ ions at a flux of 1.32 x 10^{12} ions / cm^2 / second to a fluence of 1.5 x 10^{15} ions / cm^2. During exposure to ion-irradiation the specimens were held at a range of temperatures between 300 and 600 K.

2.8 Stopping and Range of Ions in Matter (SRIM)

For the calculation of ion-irradiation-induced damage depth profiles and to convert critical dose of amorphisation results from ions / cm^2 to displacements per atom (dpa) the simulation software package SRIM (Stopping and Range of Ions in Matter) was utilised [27]. The SRIM simulations were carried out using the "Ion distribution and quick calculation of damage" mode (based on Kinchin Pease model [28]) with the ion and energy set to Kr or Se 1 MeV for *in-situ* and *ex-situ* calculations respectively. The density input was based on calculations from structural refinements, displacement threshold energies set to 50 eV [29], and lattice binding energy to 0 eV [30].

The Norgett, Robinson and Torrens model (NRT) is broadly accepted as the international standard for calculating dpa [31] and is used for damage-vacancy calculations in this study. The NRT model calculation of stable Frenkel pairs produced by primary knock on atoms is given by the formula:

$$\nu_{(NRT)} = 0.8\ {}^{T_{dam}}/_{2E_d} \qquad (2)$$

T_{dam} is the damage energy produced from primary knock on atoms (PKA) with kinetic energy E_{PKA}, and E_d is the displacement threshold energy (the minimum energy required in a collision to displace an atom and create a stable Frenkel pair). The damage energy can be calculated from SRIM outputs whilst displacement threshold energy was estimated from published data.

Issues have been identified with overestimating damage by using the NRT model with the SRIM approach and this is thoroughly covered in a previous study by Stoller *et al*. [30]. However, provided the approach for calculating dpa is kept consistent, it will be sufficient for the purpose of comparing D_c values between the range of compounds, the *in-situ* and *ex-situ* approaches and different ions used. Once the vacancies have been calculated from the SRIM output using the NRT model, the dpa can be calculated based on the number density of the target material.

3 Results

3.1 Crystallography

The single phase nature for the series of materials studied was initially confirmed using backscattered images collected via SEM, which showed no variations in grey-scale except where pores were present. The material homogeneity was further confirmed within the SEM via energy dispersive x-ray (EDX) spot analysis. The elemental stoichiometry of lanthanides to titanium was measured and its consistency tested by multiple measurements from various grains. In all cases, the matrix phase was found to be homogeneous and to consist of the desired stoichiometry. The cation ratios were calculated in Inca using the Cliff-Lorimer method. The elemental stoichiometry was calculated again using the same approach within the TEM with results attained via the SEM and TEM being comparable.

An example of one of the backscattered electron images for the Ho_2TiO_5 specimen is shown in Figure 1 to highlight the homogeneity, evident as a constant grey level across the observed area. Any darker areas in this image are pores, where this was confirmed via collection of secondary electron images showing topography.

The powder neutron diffraction data of Ho_2TiO_5 was refined using the pyrochlore structure, space group $Fd\bar{3}m$. For laboratory based powder-XRD of the $Ho_{(x)}Yb_{(2-x)}TiO_5$ (x = 1.6, 1.2, 1, 0.8. 0.4, 0) series and Er_2TiO_5, structural refinement was carried out using the fluorite structure, space group $Fm\bar{3}m$. The neutron diffraction data are overlaid with the refined calculated fit (Figure 2) with the goodness of fit displayed below the diffraction pattern as the residual plot (the difference between observed and calculated values).

The neutron powder diffraction data (Figure 2) shows broad peaks and some broad humps in the background signal. Whilst Ho_2TiO_5 has been refined using the pyrochlore structure in this study the structure of this compound has in-fact been shown to consist of long-range defect-fluorite and short-range defect-pyrochlore in previous studies[13,14]. It is the size of these pyrochlore-like domains, of the order of nanometres, that gives rise to the broad peaks and background observed here.

The refined atomic co-ordinates, isotropic thermal parameters, and lattice parameter for the Ho_2TiO_5 specimen are shown in Table 1. The details of the structural refinement in this study is in agreement with that found by Lau *et al*. where Ho_2TiO_5 was fabricated in two ways; via the floating zone furnace approach and by heating to 1700 °C followed by rapid quenching [14]. Both fabrication approaches resulted in the formation of Ho_2TiO_5 with pyrochlore structure, however there was variation in the cell parameter and oxygen x(48f) position. Some of this variation can be attributed to the pyrochlore-like domain size, which is dependent on the sintering conditions applied.

The unit cell parameters for each of the compounds were analysed via Rietveld refinement (see Table 2). A linear fit to the refined unit cell parameters versus the average lanthanide radius showed a general linear trend. To include the cell parameter of Ho_2TiO_5 in this fit, the cell parameter value was halved. This is based on the pyrochlore structure being a 2 x 2 x 2 superstructure of fluorite. Based on this fit, the unit cell parameter may be estimated via the following formula:

$$a = 1.80318 \times (r_{Ln}) + 3.31784$$

where r_{Ln} is the average lanthanide radius (ionic radii sizes were based on lanthanide being in a 3+ oxidation state and eight co-ordinated with values taken from Shannon's table of ionic radii [32]). The goodness of linear fit gave a Pearson's r value of 0.9899 indicating a good general linear trend.

Plots of the XRD data (as shown in Figure 3) show the presence of reflections related to the pyrochlore structure only for the Ho_2TiO_5 specimen. This is highlighted within the Figure 3 inset where the pyrochlore (1 1 1) reflection only appears in the lowest diffraction pattern (diffraction data for the Ho_2TiO_5 specimen).

The general trend of decreasing cell parameter value with decreasing lanthanide radius size is shown via the trend of shifting reflections to higher angles with greater ytterbium content (the ytterbium ionic radius is smaller when compared with holmium). The Er_2TiO_5 powder diffraction pattern has reflections that align well with those of $Ho_{1.2}Yb_{0.8}TiO_5$. The averaged lanthanide radius for the $Ho_{1.2}Yb_{0.8}TiO_5$, r_{Ln} = 1.003, matches well with that of Er_2TiO_5, r_{Ln} = 1.004.

Whilst the x-ray diffraction patterns indicate fluorite-type symmetry for all compounds studied except Ho_2TiO_5, further investigation via TEM selected area electron diffraction reveals reflections related to pyrochlore for the entire series (Figure 4). All the patterns contain the long-range fluorite structure indicated by the brightest reflections, however less intense additional reflections indicate the presence of a slightly modulated short-range pyrochlore structure.

Figure 4 (i) is a simulated diffraction pattern for a pyrochlore-structured crystal, space group *Fd*$\bar{3}$*m*, viewed down zone axis [1 1 0]. The SAEDs for the

$Ho_{(x)}Yb_{(2-x)}TiO_5$ series and Er_2TiO_5 (Figures 4 (a to h)) all show the characteristic pyrochlore (1 1 1) reflection as viewed down zone axis [1 1 0]. The (1 1 1) reflection for this series becomes more diffuse and elongated with greater ytterbium concentration. This change in the reflections' intensity distribution may be attributed to a decreasing pyrochlore domain size from Ho_2TiO_5 to Yb_2TiO_5. This domain size difference has been noted before in a neutron diffraction study by Lau *et al*. [13] where larger ordered pyrochlore domains were determined for Ho_2TiO_5 (3 nm) when compared with Yb_2TiO_5 (2 nm).

In a previous study, nano-domains of pyrochlore structure in long-range fluorite structure for Yb_2TiO_5 were found using high resolution electron microscopy images combined with inverse fast Fourier transforms [16].

There is also a higher level of structural complexity evident in the SAED's in Figures 4 (a) and (b) for the Ho_2TiO_5 and $Ho_{1.6}Yb_{0.4}TiO_5$ compounds respectively. There appears to be structural modulation from the ideal pyrochlore structure, evident by the presence of 2 extra reflections in the (1 1 1) directions, and 6 extra reflections in the (6 6 2) directions, indicating 3-fold and 7-fold increases in the unit cell in the (1 1 1) and (6 6 2) directions respectively.

The combined x-ray diffraction and TEM results show the presence of long-range fluorite structure combined with short-range pyrochlore domains in all of the phases tested. There appears to be a trend of decreasing pyrochlore ordering with increasing ytterbium concentration and decreasing lanthanide radius, as evidenced with the Er_2TiO_5 compound. Greater disordering of the pyrochlore towards the fluorite structure has previously been associated with

greater resistance to ion-irradiation induced amorphisation. The ion-irradiation response is analysed in the following section.

3.2 Critical temperature of crystallinity, T_c, based on the *in-situ* TEM approach

For this study Ho_2TiO_5, $HoYbTiO_5$, Yb_2TiO_5 and Er_2TiO_5 specimens were irradiated *in-situ* within the TEM using 1 MeV Kr^{2+} ions to a fluence sufficient to facilitate the phase transition from crystalline to amorphous. The evolution of ion-induced damage was monitored, using the TEM, via collection of SAEDs. The loss of Bragg diffraction maxima within the SAEDs and subsequent replacement with diffuse rings was indicative of the crystalline to amorphous transition. Ion-irradiation was repeated at various temperatures ranging from 50 to 700 K. The plot of the measured critical dose of amorphisation, D_c, versus temperature is displayed in Figure 5. For each of the four compounds tested there is a critical temperature above which the D_c significantly increases, i.e., the ion-irradiation-induced damage is annealed at a sufficient rate to maintain at least some crystallinity within the tested grains. This critical temperature, T_c, represents a point where the desired crystal structure and its associated properties can be maintained regardless of the irradiating ion fluence. A lower T_c is therefore a desirable characteristic for ceramics in nuclear applications.

The calculated values D_{c0}, critical dose of amorphisation at 0 K, and T_c from the data plotted in Figure 5 are displayed in Table 3. There is an improvement in radiation response, T_c, across the Ho_2TiO_5, $HoYbTiO_5$ and Yb_2TiO_5 series.

This trend of decreasing T_c is correlated with a decrease in average lanthanide radius.

The T_c values decrease from Ho_2TiO_5 to Er_2TiO_5 to $HoYbTiO_5$ to Yb_2TiO_5. Er has a very similar cation ionic radius to HoYb in the Ln_2TiO_5 compounds (radius of Er^{3+}(VIII) = 1.004 Å, $(HoYb)^{3+}$ (VIII) = 1.00 Å) based on ionic radii table values from Shannon [32]. According to the values shown in Table 3, Er has a slightly greater ionic radius than the average radius of HoYb and Er also has a greater T_c value. This supports the general trend of decreasing T_c with decreasing lanthanide ionic radii size. This matches the radiation tolerance trend previously found for Y_2TiO_5, $YYbTiO_5$ and Yb_2TiO_5 where it was also shown that the Ln_2TiO_5 compounds had greater D_c and lower T_c values relative to their corresponding $Ln_2Ti_2O_7$ pyrochlores [7].

However, the general trend of decreasing T_c with decreasing lanthanide radius is not fully consistent across the entire series of Ln_2TiO_5 compounds (Figure 6). The data displayed in Figure 6 is compiled from various studies, including exclusively Ln_2TiO_5 compounds with orthorhombic symmetry [5]. When a material is exposed to high energy particles the particle - lattice atom interactions can lead to phase transitions, including amorphisation. Liu *et al*. [33] used density functional theory first principles calculations to determine the point defect formation energies for a series of Ln_2TiO_5 compounds with orthorhombic symmetry. They found that the Ln2-Ti anti-site, followed by the Ln1-Ti anti-site defects, were the most energetically favourable defect types formed. The formation energies for the Ln2-Ti anti-site defects decreased with increasing lanthanide cation radius from yttrium and holmium to neodymium, and then increased from neodymium to lanthanum. This defect formation

energy trend matched the experimentally-determined ion-irradiation tolerance trend, as defined by T_c, found by Aughterson *et al*. [5], where T_c increased from dysprosium to neodymium and fell slightly from neodymium to lanthanum (as shown in Figure 6).

Tracy *et al*. [4] showed that a decrease in the lanthanide radius size occupying the Ln_2TiO_5 orthorhombic symmetry A-site resulted in decreasing damage track widths when exposed to 1.47 GeV Xe ions. In this series, Ln_2TiO_5 (Ln = La, Nd, Sm, Gd), the decrease in damage area with smaller lanthanides was attributed to an increase in epitaxial recrystallisation from the outer edges of the damage zone toward the amorphous centre. High resolution TEM showed the presence of defect-fluorite structure in the outer recrystallisation zone of Sm_2TiO_5, whilst La_2TiO_5 was found to be completely amorphous across its damage zone. A similar study by Zhang *et al*. [34] where swift heavy ions, 2.2 GeV Au ions, were used to irradiate a specimen of Gd_2TiO_5 showed the same epitaxial recrystallisation from the outer edge of the damage zone, however in this case a transition from the orthorhombic to hexagonal symmetry was observed in the recrystallisation zone.

The experimental observation that Ln_2TiO_5 compounds with orthorhombic symmetry are capable of transitioning to other symmetries shows that the defect formation energies and subsequent defect accumulation are not the only things that need to be considered. When analysing ion-irradiation response, it is also necessary to consider the ability to form other structure types. The temperature stability diagram proposed by Shepelev and Petrova [11] may give some indication of potential phase transitions available to Ln_2TiO_5

compounds exposed to ion-irradiation. In the case of Gd_2TiO_5 there is a low temperature orthorhombic and higher temperature hexagonal phase and this fits well with the ion-irradiation induced phase transition observed by Zhang *et al*. [34]. However the orthorhombic to defect-fluorite symmetry transition of Sm_2TiO_5 observed by Tracy *et al*. [4] does not fit with the proposed temperature stability diagram. It should be noted that symmetries others than those shown in the Shepelev and Petrova temperature stability diagram have been shown to form at higher pressure sintering. In a study by Zhang *et al*. [35] using high pressure, La_2TiO_5 transitioned from orthorhombic to hexagonal symmetry at 10 GPa, and Nd_2TiO_5 underwent the same transition at 12.9 GPa.

The swift heavy ion irradiation that induced phase transitions were dominated by inelastic, electronic scattering. This is different from the ion – lattice atom interactions that occurred within this study. The use of 1 MeV Kr ions has resulted in scattering dominated by elastic interactions, as highlighted by the electronic to nuclear stopping ratios (Table 3) with values less than 1.

In our previous work [5] bulk Dy_2TiO_5 with orthorhombic symmetry was irradiated with 12 MeV Au ions and the structure analysed using grazing incidence x-ray diffraction. No intermediate phase transition was detected between the crystalline, orthorhombic symmetry, to an amorphous phase. It is therefore proposed that, for heavy ion irradiation around the low MeV energy range, which is dominated by elastic scattering, it may be sufficient to use the defect formation energy calculations to predict trends within the Ln_2TiO_5 series.

As the lanthanide radius becomes smaller, beyond Dy, the ion-irradiation response, T_c, improves, i.e. lowers in value (Figure 6). This region coincides with Ln_2TiO_5 compounds with cubic symmetry. It has been noted in previous studies that Ln_2TiO_5 compounds with cubic symmetry tend to display improved ion-irradiation tolerance [7,8]. For this series, it appears that the ability to tolerate disorder within the structure is the driver of ion-irradiation tolerance. In particular, the trend from the more ordered pyrochlore structure of Ho_2TiO_5 to the disordered, no preferred cation site and anion disorder, of the fluorite structured Yb_2TiO_5 coincides with an improvement in radiation response. Whilst there have been no defect formation energy studies of the cubic Ln_2TiO_5 series, there have been many studies on the related pyrochlore $Ln_2Ti_2O_7$ series.

As covered in the introduction, smaller lanthanides, due to their size being closer to that of titanium, can accommodate Ln-Ti anti-site disordering, and so the defect-fluorite structure will be more thermodynamically stable. It is this stability of the fluorite structure that has been linked with improved radiation tolerance. In a comprehensive review of T_c values for pyrochlore and fluorite structured materials with $Ln_2M_2O_7$ (M = Ti, Mo, Sn, Hf, and Zr) by Lumpkin *et al*. [17], a general, although not linear, trend was found between radiation tolerance and the tendency toward the fluorite structure. It should be noted that other characteristics such as local bonding and disordering energies were also shown to contribute to the correlations found between T_c values and characteristics.

In a similar study to this one, Whittle *et al*. [7] showed that the sequential improvement in T_c from Y_2TiO_5 to $YYbTiO_5$ to Yb_2TiO_5 could be related to the

increase in disordering on the cation site toward Yb_2TiO_5. This trend is also observed here (Figure 6). The $Ho_{(x)}Yb_{(2-x)}TiO_5$ series of diffraction patterns shown in Figure 4 lend extra evidence to the order (presence of distinct ordered pyrochlore phase in Ho_2TiO_5) to disorder (very diffuse scattering from the modulated pyrochlore phase in Yb_2TiO_5) phase trend as extra ytterbium is added to the stoichiometry. This suggests that the ability to incorporate greater cation and anion disorder into the structure significantly improves the radiation response.

Sickafus *et al*. [36] showed a correlation between the order–disorder defect reaction pair (cation anti-site plus anion Frenkel defect) energy in the $Ln_2Zr_2O_7$ pyrochlore and $Ln_4Zr_3O_{12}$ δ-phase series, and the pyrochlore or δ-phase-to-fluorite phase transition temperature. They therefore suggested that temperature–composition phase diagrams can be used to predict the ion-irradiation induced phase transitions from ordered to disordered (defect-fluorite) structures. Another study by Jiang *et al*. [37] also showed a strong correlation between the calculated energetics for the ordered-pyrochlore-to-disordered-fluorite transition and the corresponding phase transition temperatures obtained from phase diagrams. Of greatest relevance to this study, the related $Ln_2Ti_2O_7$ pyrochlore series was shown to have non-monotonic behaviour for the caclulated disorder energies. The trend of increasing and then decreasing disorder energy with increasing lanthanide size correlated well with their experimentally determined radiation response T_c values [38].

The opposite trends are found for the Ln_2TiO_5 orthorhombic and cubic systems. That is, a lower defect formation energy resulted in greater

susceptibility to amorphisation in the orthorhombic system, whilst the cubic system has a correspondingly greater resistance to amorphisation. This is attributed to the lattice energy created by incorporation of defects versus the amorphous system energy. For those systems where it is energetically favourable to accommodate defects such as cation anti-sites and anion Frenkel disorder (which is the case for the fluorite structure) a stable crystalline system can be maintained. In contrast, accumulation of defects in the orthorhombic system creates energetic instabilities leading to eventual amorphisation.

3.3 Amorphisation versus temperature trends for bulk irradiated samples.

Cross-sectional TEM is a useful tool for assessing damage depth profiles and/or amorphous volumes in bulk irradiated materials. By using either micro-diffraction or SAED to analyse the ion-irradiation damage induced layers, crystalline phase changes can be detected[23,39], including the crystalline to amorphous phase transition. Here we undertake a systematic temperature study of ion-irradiation response by using cross-section. Figure 7 is a series of cross-sectional TEM bright field images that show the damage depth profiles for the Yb_2TiO_5 specimen held at 300, 400 and 450 K whilst being irradiated with 1 MeV selenium ions to a fluence of 1.5 x 10^{15} ions / cm^2. For the irradiation carried out at ambient temperature (figure 7 (a)) this fluence was sufficient to create a completely amorphous layer from the surface down to just over 400 nm depth. The crystallinity of all cross-sectional specimens was analysed using nano-diffraction (beam of ~ 25 nm width) at multiple

points across the entire damage depth. The use of diffraction allowed the amorphous depth to be determined.

In order to ensure that the *in-situ* experiments, conducted using Kr ions, give displacements comparable to the *ex-situ* experiments, conducted using Se ions, SRIM was used to calculate damage depth profiles and the results are shown in figure 8. For best comparison between the two approaches very similar damage depth profiles should be used and this has been achieved. It should be noted here that the SRIM calculated lattice atom displacements are based purely on elastic, nuclear scattering whilst electronic scattering only contributes to ion-energy loss in the SRIM simulation approach.

To compare the *in-situ* and *ex-situ* ion-irradiation results, ideally the D_c would be determined from the top 200 nm of the bulk irradiated sample (the approximate maximum thickness for *in-situ* specimens). However, for the *ex-situ* ion-irradiation, the fluence was set to a value (1 MeV Se^+, 1.5 x 10^{15} ions / cm^2) sufficient to facilitate the crystalline to amorphous transition based on where the *in-situ* D_c values had previously been observed to significantly increase (Figure 5). This results in data that will show whether the 1.5 x 10^{15} ions / cm^2 has rendered the top 200 nm amorphous, but does not allow the D_c from the top 200 nm to be determined. An incremental increase in dose followed by intermittent cross-sectional analysis would theoretically allow the D_c value to be determined. This would be an extremely time-consuming experiment, and undertaking a systematic series of such experiments is almost unfeasible.

The amorphous region of the bulk specimen is large (~ 400 nm) for irradiations carried out at 300 K (Figure 7) and the D_c is determined from the

final depth of the amorphous volume. The experimentally-determined amorphous depth was compared with the SRIM based calculations for the damage depth profiles (Figure 8) and from this a D_c value was determined (Table 4).

Figure 8 reveals that the damage depth profile has an increasing gradient from the surface to 200 nm depth. To determine the *in-situ* D_{c300K}, the lowest dpa value across the 200 nm damage depth is used, as this is the minimum damage required to render the entire grain amorphous (Table 4).

As the temperature of the bulk specimens became closer to the *in-situ* T_c value, domains of crystallinity begin to appear in the vicinity of the top 200 nm volume (Figure 7). The specimens were classified as having reached their critical temperature if there was a general trend of crystallinity detected within the various sampled top 200 nm regions, i.e. at least 2 out of 5 regions tested showed some crystallinity (T_c values shown in Table 4).

The determination of dpa using the two experimental approaches differs in several aspects. With the TEM *ex-situ* cross-sectional approach, the amorphous depth is measured and a dpa value can be selected directly from the damage depth profile generated by SRIM. At a depth of approximately 500 nm, the irradiating ion will have reached close to its complete trajectory and during the process will have lost significant kinetic energy. This lower energy ion will have ion – lattice atom interactions strongly dominated by elastic scattering, much more than within the top 200 nm from the surface. This results in fundamentally different ion – lattice atom scattering creating the damage in the observed specimens between the *in-situ* and *ex-situ* experimental approaches. The greater elastic scattering, which tends to give

greater displacement density, near the 500 nm depth should result in a lower D_c value for the *ex-situ,* when compared with the < 200 nm thick specimen *in-situ* approach, where there is greater inelastic scattering.

For bulk-irradiated materials there is added complexity from the ballistic mixing of the irradiating ions, resulting in accumulation within the lattice. This ballistic mixing is not an issue for the *in-situ* TEM specimens as the specimens are thin enough so that the trajectory of the irradiating ions normally results in complete transmission. This ballistic mixing within the bulk material, which introduces a new element into the matrix either via interstitials or lattice atom replacement, will likely destabilise the local structure and should result in a lowering of the D_c value for the *ex-situ* approach.

There are significant differences in the $D_{c(300K)}$ values attained using the two different approaches (Table 4). These differences in values may be due to the differences in experimental set-up described above but may also be due to the energetic differences in the systems between the large surface area to volume ratio found for the thin *in-situ* specimens when compared to the bulk material. These thin *in-situ* specimens allow defects to more easily migrate to the surface, especially at elevated temperatures where defects have greater mobility. It may be expected that the $D_{c(300K)}$ values attained using the *ex-situ* approach would differ when compared with the *in-situ* due to factors already discussed, higher elastic scattering, ballistic mixing and lower surface area to volume ratio. The Yb_2TiO_5 specimen has a significantly higher *ex-situ* $D_{c(300K)}$ value compared with the *in-situ* and this may be explained by the ambient temperature being close to the T_c and for bulk specimens epitaxial recrystallisation is enhanced. Overall, the same trend of increasing $D_{c(300K)}$

value with increasing ytterbium content is found by both experimental approaches.

Previous studies of Ln_2TiO_5 specimens exposed to high energy, GeV, ions have shown that epitaxial recrystallisation occurs within the damage zone for some of the smaller ionic radii lanthanides[4,34]. The lower T_c values determined for the bulk samples in our study are proposed to be due to enhanced epitaxial recrystallisation. In the bulk material, the lattice beyond the damage zone can act as a nucleation point for recrystallisation at the ion-irradiated damage zone / crystalline interface. In each TEM cross-sectional temperature versus damage depth profile series (e.g. Figure 7), crystalline domains are observed within the damage zone with increasing temperature, beginning from the damage zone / crystalline interface upwards toward the surface. This crystallinity from the bottom up is despite the fact that the greatest concentration of ion-irradiation induced defects occurs at around the 200 ± 100 nm depth (Figure 8). If epitaxial recrystallisation was not a factor in crystallinity recovery, recrystallisation would be expected to occur initially at the deepest point amorphisation had occurred, followed by the surface, and finally at around the 200 nm depth where the greatest concentration of defects should be found.

As with the D_c values found using the two different approaches, the T_c values are significantly different, with lower values observed when using the bulk irradiation approach (Table 4). However, the trend of a lower T_c value with greater ytterbium content is consistent across the two approaches used.

The proposed mechanism for improved radiation tolerance for the Ln_2TiO_5 cubic compounds with smaller lanthanides is the ability to accommodate

cation anti-site disordering into the crystalline structure. Investigation of the cross-sectional damage zone using nano-beam diffraction (NBD) has shown the presence of defect-fluorite and defect-pyrochlore regions (Figure 7 b) within the recrystallisation zone of Yb_2TiO_5 held at 400 K during irradiation. The lack of diffuse rings found in these NBD patterns indicates a high degree of crystallinity and gives confidence that the observed phase change from defect-pyrochlore to defect-fluorite is real. The ability of Yb_2TiO_5 to transition from a long-range defect-fluorite, short-range defect-pyrochlore to defect-fluorite upon irradiation gives validation to this mechanism for improved ion-irradiation response.

Concluding remarks

An investigation of the ion-irradiation response for the Ho_2TiO_5, $HoYbTiO_5$, Er_2TiO_5, and Yb_2TiO_5 cubic symmetry series of compounds revealed a trend by which compounds containing the smaller lanthanides are more radiation tolerant. This trend is consistent with previous studies of the related pyrochlore structured $Ln_2Ti_2O_7$ series of compounds.

The improved radiation resistance is related to lower disordering energies (cation anti-site energy) and greater defect mobility for Ln_2TiO_5 compounds containing lanthanides with a smaller radius. The greater defect mobility allows epitaxial recrystallization of the damage zone to occur.

In-situ TEM irradiation was compared to results from *ex-situ* ion irradiation followed by TEM cross-sections. The T_c values attained using the *in-situ* approach tended to be higher relative to the *ex-situ* values. There were several possible mechanisms described for this variation in values between

characterisation techniques with epitaxial recrystallisation for irradiated bulk specimens being proposed as the source of lower T_c values found using the *ex-situ* approach. Whilst values were different the trends in both the D_c and T_c values match between the *in-situ* and *ex-situ* experimental approaches.

Conflicts of Interest

There are no conflicts of interest to declare.

Acknowledgements

The electron microscopy with *in-situ* ion-irradiation was accomplished at Argonne National Laboratory at the IVEM-Tandem Facility, a U.S. Department of Energy Facility funded by the DOE Office of Nuclear Energy, operated under Contract No. DE-AC02-06CH11357 by UChicago Argonne, LLC. The authors wish to acknowledge the help and support of the staff at the IVEM-Tandem facility, in particular Marques Kirk, Peter Baldo, and Edward Ryan.

References

1 VD Risovany, EE Varlashova, and DN Suslov, "Dysprosium titanate as an absorber material for control rods," Journal of Nuclear Materials **281** (1), 84-89 (2000).

2 H. S. Kim, C. Y. Joung, B. H. Lee, S. H. Kim, and D. S. Sohn, "Characteristics of GdxMyOz (M = Ti, Zr or Al) as a burnable absorber," Journal of Nuclear Materials **372** (2-3), 340-349 (2008).

3 D. Y. Yang, C. P. Xu, E. G. Fu, J. Wen, C. G. Liu, K. Q. Zhang, Y. Q. Wang, and Y. H. Li, "Structure and radiation effect of Er-stuffed pyrochlore Er2(Ti2−xErx)O7−x/2 (x = 0–0.667)," Nuclear Instruments and Methods in Physics Research Section B: Beam Interactions with Materials and Atoms **356–357**, 69-74 (2015).

4 C.L Tracy, Liang, M., Zhang, J., Zhang, F., Wang, Z., Ewing, R.C., "Structural response of A2TiO5 (A=La, Nd, Sm, Gd) to swift heavy ion irradiation," Acta Materialia **60** (11), 4477-4486 (2012).

5 Robert D. Aughterson, Gregory R. Lumpkin, Mihail Ionescu, Massey de los Reyes, Baptiste Gault, Karl R. Whittle, Katherine L. Smith, and Julie M. Cairney, "Ion-irradiation resistance of the orthorhombic Ln2TiO5

(Ln = La, Pr, Nd, Sm, Eu, Gd, Tb and Dy) series," Journal of Nuclear Materials **467, Part 2**, 683-691 (2015).

6 Jiaming Zhang, Fuxiang Zhang, Maik Lang, Fengyuan Lu, Jie Lian, and Rodney C. Ewing, "Ion-irradiation-induced structural transitions in orthorhombic Ln2TiO5," Acta Materialia **61** (11), 4191-4199 (2013); K. R. Whittle, G. R. Lumpkin, M. G. Blackford, R. D. Aughterson, K. L. Smith, and N. J. Zaluzec, "Ion-beam irradiation of lanthanum compounds in the systems La2O3-Al2O3 and La2O3-TiO2," Journal of Solid State Chemistry **183** (10), 2416-2420 (2010).

7 Karl R. Whittle, Mark G. Blackford, Robert D. Aughterson, Gregory R. Lumpkin, and Nestor J. Zaluzec, "Ion irradiation of novel yttrium/ytterbium-based pyrochlores: The effect of disorder," Acta Materialia **59** (20), 7530-7537 (2011).

8 RD Aughterson, GR Lumpkin, M de los Reyes, B Gault, P Baldo, E Ryan, KR Whittle, KL Smith, and JM Cairney, "The influence of crystal structure on ion-irradiation tolerance in the Sm (x) Yb (2-x) TiO 5 series," Journal of Nuclear Materials **471**, 17-24 (2016).

9 G. Panneerselvam, R. V. Krishnan, M. P. Antony, K. Nagarajan, T. Vasudevan, and P. R. V. Rao, "Thermophysical measurements on dysprosium and gadolinium titanates," Journal of Nuclear Materials **327** (2-3), 220-225 (2004).

10 A. Sinha and B. P. Sharma, "Development of dysprosium titanate based ceramics," Journal of the American Ceramic Society **88** (4), 1064-1066 (2005).

11 Y. F. Shepelev and M. A. Petrova, "Crystal Structures of Ln(2)TiO(5) (Ln = Gd, Dy) Polymorphs," Inorganic Materials **44** (12), 1354-1361 (2008).

12 G. C. Lau, B. D. Muegge, T. M. McQueen, E. L. Duncan, and R. J. Cava, "Stuffed rare earth pyrochlore solid solutions," Journal of Solid State Chemistry **179** (10), 3126-3135 (2006).

13 G. C. Lau, T. M. McQueen, Q. Huang, H. W. Zandbergen, and R. J. Cava, "Long- and short-range order in stuffed titanate pyrochlores," Journal of Solid State Chemistry **181** (1), 45-50 (2008).

14 G. C. Lau, R. S. Freitas, B. G. Ueland, M. L. Dahlberg, Q. Huang, H. W. Zandbergen, P. Schiffer, and R. J. Cava, "Structural disorder and properties of the stuffed pyrochlore Ho2TiO5," Physical Review B **76** (5) (2007).

15 A. V. Shlyakhtina, D. A. Belov, S. Yu Stefanovich, and L. G. Shcherbakova, "Nanostructuring phenomena in oxygen-conducting complex oxides of heavy REE," Russ J Electrochem **47** (5), 620-627 (2011).

16 Robert D. Aughterson, Gregory R. Lumpkin, Massey de los Reyes, Neeraj Sharma, Christopher D. Ling, Baptiste Gault, Katherine L. Smith, Maxim Avdeev, and Julie M. Cairney, "Crystal structures of orthorhombic, hexagonal, and cubic compounds of the Sm(x)Yb(2−x)TiO5 series," Journal of Solid State Chemistry **213** (0), 182-192 (2014).

17 G. R. Lumpkin, M. Pruneda, S. Rios, K. L. Smith, K. Trachenko, K. R. Whittle, and N. J. Zaluzec, "Nature of the chemical bond and prediction

of radiation tolerance in pyrochlore and defect fluorite compounds," Journal of Solid State Chemistry **180** (4), 1512-1518 (2007).

18 GR Lumpkin, EJ Harvey, KL Smith, MG Blackford, and NJ Zaluzec, "Radiation Tolerance of A2Ti2O7 Compounds at the Cubicmonoclinic Boundary", in *Pacific Basin Nuclear Conference (15th : 2006 : Sydney, Australia)* (Australian Nuclear Association, Sydney, N.S.W., 2006), pp. [703]-[709]; R. C. Ewing, J. Lian, and L. M. Wang, "Ion Beam-Induced Amorphization of the Pyrochlore Structure-Type: A Review," MRS Online Proceedings Library **792**, null-null (2003); S. X. Wang, L. M. Wang, R. C. Ewing, and K. V. G. Kutty, "Ion irradiation of rare-earth- and yttrium-titanate-pyrochlores," Nuclear Instruments & Methods in Physics Research Section B-Beam Interactions with Materials and Atoms **169**, 135-140 (2000); Jie Lian, L. M. Wang, Kai Sun, and Rodney C. Ewing, "In situ TEM of radiation effects in complex ceramics," Microsc Res Techniq **72** (3), 165-181 (2009).

19 J. Lian, L. M. Wang, R. C. Ewing, and L. A. Boatner, "Ion beam implantation and cross-sectional TEM studies of lanthanide titanate pyrochlore single crystals," Nuclear Instruments & Methods in Physics Research Section B-Beam Interactions with Materials and Atoms **241** (1-4), 365-371 (2005).

20 JA Hinks, "A review of transmission electron microscopes with in situ ion irradiation," Nuclear Instruments and Methods in Physics Research Section B: Beam Interactions with Materials and Atoms **267** (23), 3652-3662 (2009).

21 J. S. Williams, Xianfang Zhu, M. C. Ridgway, M. J. Conway, B. C. Williams, F. Fortuna, M.-O. Ruault, and H. Bernas, "Preferential amorphization and defect annihilation at nanocavities in silicon during ion irradiation," Applied Physics Letters **77** (26), 4280-4282 (2000); P. D. Edmondson, D. J. Riley, R. C. Birtcher, and S. E. Donnelly, "Amorphization of crystalline Si due to heavy and light ion irradiation," Journal of Applied Physics **106** (4), 043505 (2009).

22 K. E. Sickafus, Hj Matzke, Th Hartmann, K. Yasuda, J. A. Valdez, P. Chodak Iii, M. Nastasi, and R. A. Verrall, "Radiation damage effects in zirconia," Journal of Nuclear Materials **274** (1–2), 66-77 (1999).

23 K. E. Sickafus, L. Minervini, R. W. Grimes, J. A. Valdez, M. Ishimaru, F. Li, K. J. McClellan, and T. Hartmann, "Radiation Tolerance of Complex Oxides," Science **289** (5480), 748-751 (2000).

24 B Hunter, "Rietica - A Visual Rietveld Program," International Union of Crystallography Commission on Powder Diffraction **Newsletter number 20 (Summer)** (1998).

25 Marquis A. Kirk, Peter M. Baldo, Amelia C. Y. Liu, Edward A. Ryan, Robert C. Birtcher, Zhongwen Yao, Sen Xu, Michael L. Jenkins, Mercedes Hernandez-Mayoral, Djamel Kaoumi, and Arthur T. Motta, "In situ transmission electron microscopy and ion irradiation of ferritic materials," Microsc Res Techniq **72** (3), 182-186 (2009).

26 W. J. Weber, "Models and mechanisms of irradiation-induced amorphization in ceramics," Nuclear Instruments and Methods in Physics Research Section B: Beam Interactions with Materials and Atoms **166–167** (0), 98-106 (2000).

27 J. P. Biersack J. F. Ziegler, M. D. Ziegler, "SRIM The Stopping and Range of Ions in Matter," www.SRIM.org (2008).
28 GH Kinchin and RS Pease, "The displacement of atoms in solids by radiation," Reports on progress in physics **18** (1), 1 (1955).
29 Gregory R Lumpkin, Katherine L Smith, Mark G Blackford, Karl R Whittle, Elizabeth J Harvey, Simon AT Redfern, and Nestor J Zaluzec, "Ion irradiation of ternary pyrochlore oxides," Chem Mater **21** (13), 2746-2754 (2009).
30 R. E. Stoller, M. B. Toloczko, G. S. Was, A. G. Certain, S. Dwaraknath, and F. A. Garner, "On the use of SRIM for computing radiation damage exposure," Nuclear Instruments and Methods in Physics Research Section B: Beam Interactions with Materials and Atoms **310**, 75-80 (2013).
31 E521, "Standard Practice for Neutron Radiation Damage Simulation by Charged-Particle Irradiation", in *Annual Book of ASTM Standards, Vol. 12.02* (ASTM International, West Conshohocken, PA, 2009).
32 R. D. Shannon, "Revised effective ionic radii and systematic studies of interatomic distances in halides and chalcogenides," Acta Crystallographica Section A **32**, 751-767 (1976).
33 Xiao Liu, Dongyan Yang, Chenguang Liu, Huan Liu, Shiyin Ji, Pengcheng Mu, Yiyuan Wu, and Yuhong Li, "Insights into the radiation behavior of Ln2TiO5 (Ln = La-Y) from defect energetics," Comp Mater Sci **139**, 295-300 (2017).
34 J. M. Zhang, M. Lang, R. C. Ewing, R. Devanathan, W. J. Weber, and M. Toulemonde, "Nanoscale phase transitions under extreme conditions within an ion track," Journal of Materials Research **25** (7), 1344-1351 (2010).
35 F. X. Zhang, J. W. Wang, M. Lang, J. M. Zhang, and R. C. Ewing, "Pressure-induced structural transformations in lanthanide titanates: La2TiO5 and Nd2TiO5," Journal of Solid State Chemistry **183** (11), 2636-2643 (2010).
36 K. E. Sickafus, R. W. Grimes, J. A. Valdez, A. Cleave, M. Tang, M. Ishimaru, S. M. Corish, C. R. Stanek, and B. P. Uberuaga, "Radiation-induced amorphization resistance and radiation tolerance in structurally related oxides," Nat Mater **6** (3), 217-223 (2007).
37 C. Jiang, C. R. Stanek, K. E. Sickafus, and B. P. Uberuaga, "First-principles prediction of disordering tendencies in pyrochlore oxides," Physical Review B **79** (10), - (2009).
38 L. Minervini, R. W. Grimes, and K. E. Sickafus, "Disorder in pyrochlore oxides," Journal of the American Ceramic Society **83** (8), 1873-1878 (2000).
39 J. A. Valdez, M. Tang, and K. E. Sickafus, "Radiation damage effects in delta-Sc4Zr3O12 irradiated with Kr2+ ions under cryogenic conditions," Nuclear Instruments & Methods in Physics Research Section B-Beam Interactions with Materials and Atoms **250**, 148-154 (2006); M. Tang, P. Lu, J. A. Valdez, and K. E. Sickafus, "Heavy ion irradiation-induced phase transformation in polycrystalline Dy2O3," Philos Mag **86** (11), 1597-1613 (2006).
40 R. D. Aughterson, G. R. Lumpkin, M. de los Reyes, B. Gault, P. Baldo, E. Ryan, K. R. Whittle, K. L. Smith, and J. M. Cairney, "The influence of

crystal structure on ion-irradiation tolerance in the Sm(x)Yb(2-x)TiO5 series," Journal of Nuclear Materials **471**, 17-24 (2016).

41 G. R. Lumpkin R. D. Aughterson, K. L. Smith, Z. Zhang, N. Sharma, J. M. Cairney, "The crystal structures and corresponding ion-irradiation response for the Tb(x)Yb(2-x)TiO5 series," Ceram Int (in-press).

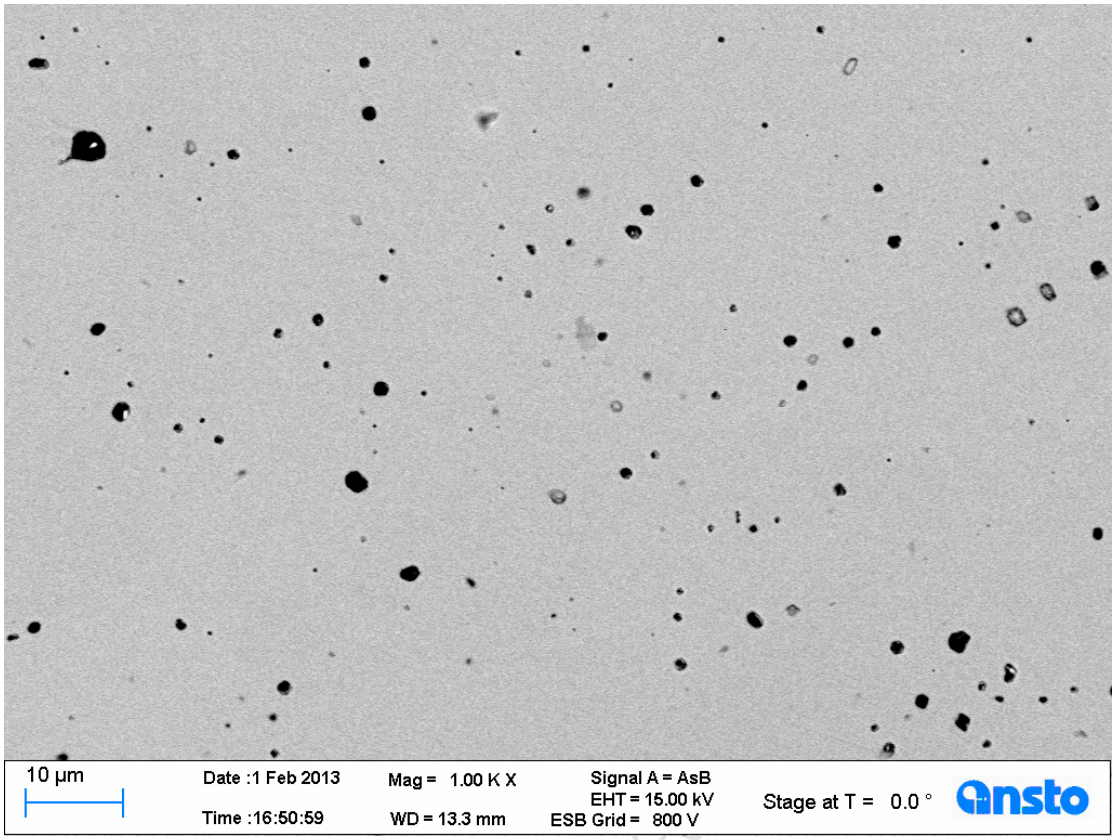

Figure 1. SEM back-scattered image of the Ho_2TiO_5 design phase. Dark spots indicate the locations of pores, whilst the constant grey-scale indicates homogeneous distribution of elements.

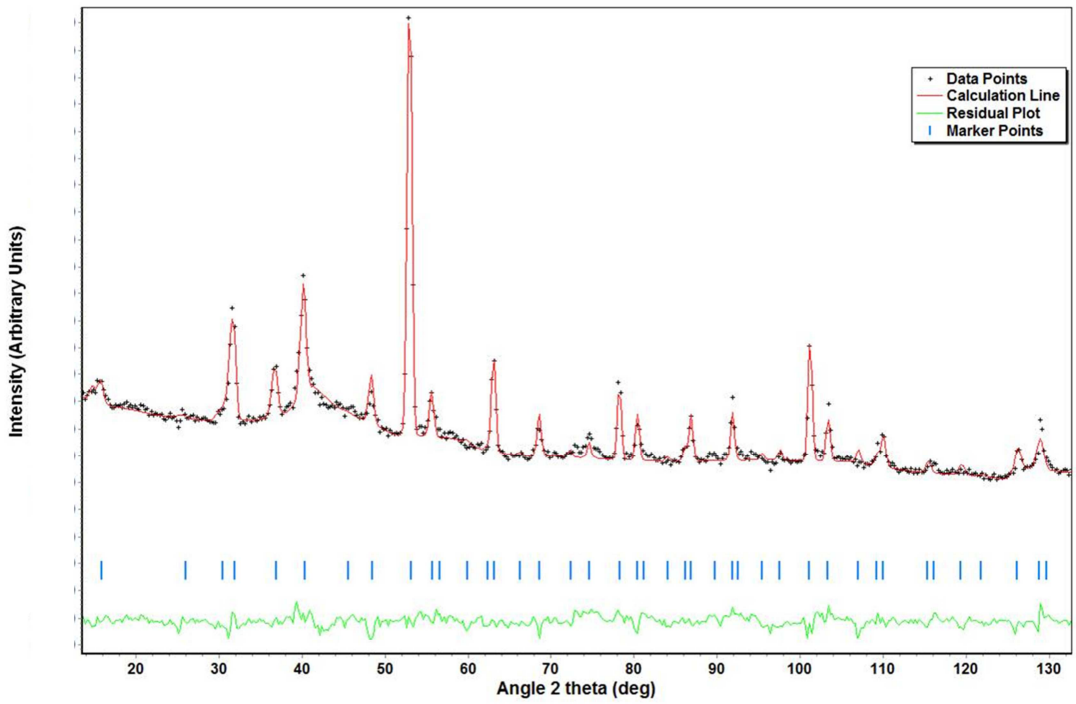

Figure 2. The observed, calculated (Rietica) and residual plot for the Ho_2TiO_5 neutron powder diffraction data. The powder diffraction data is shown as black crosses, refined calculated fit as the red trace, the difference between observed and calculated (residual plot) shown as the green trace and the reflection markers as blue vertical lines.

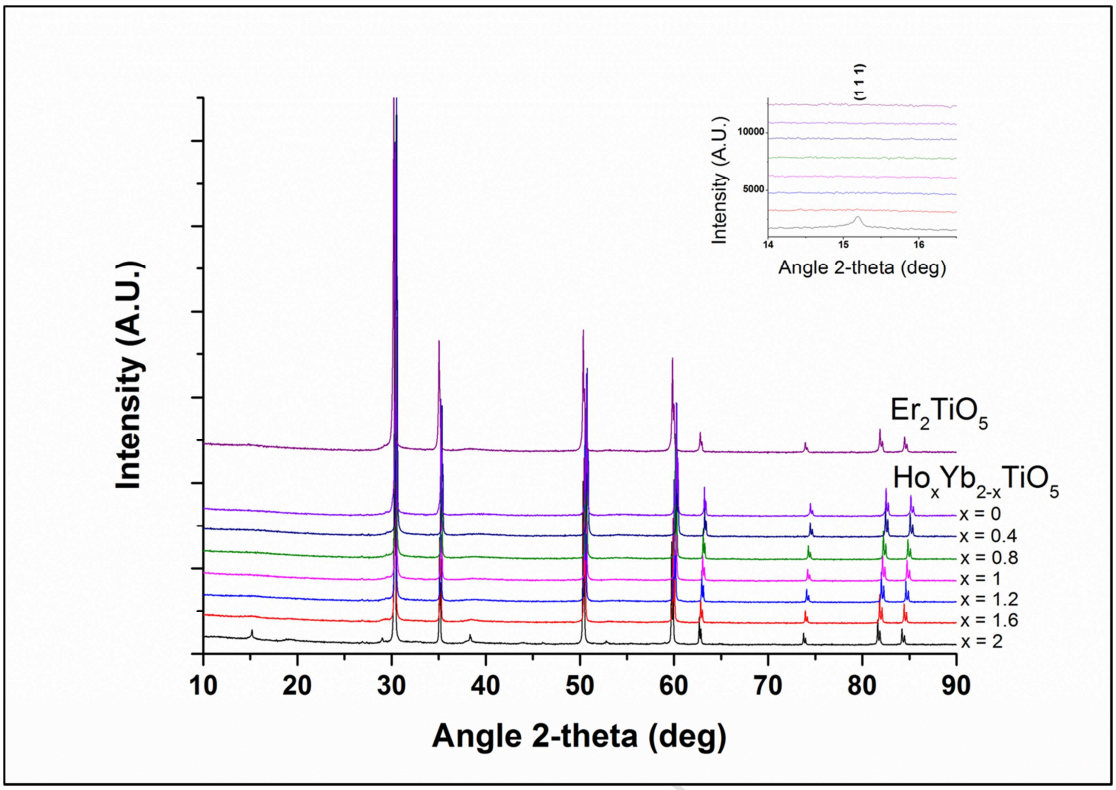

Figure 3. Laboratory powder x-ray diffraction patterns of the $Ho_{(x)}Yb_{(2-x)}TiO_5$ series and Er_2TiO_5 with $Fm\bar{3}m$ symmetry. The inset highlights the (1 1 1) pyrochlore reflection, which is only visible for the Ho_2TiO_5 sample.

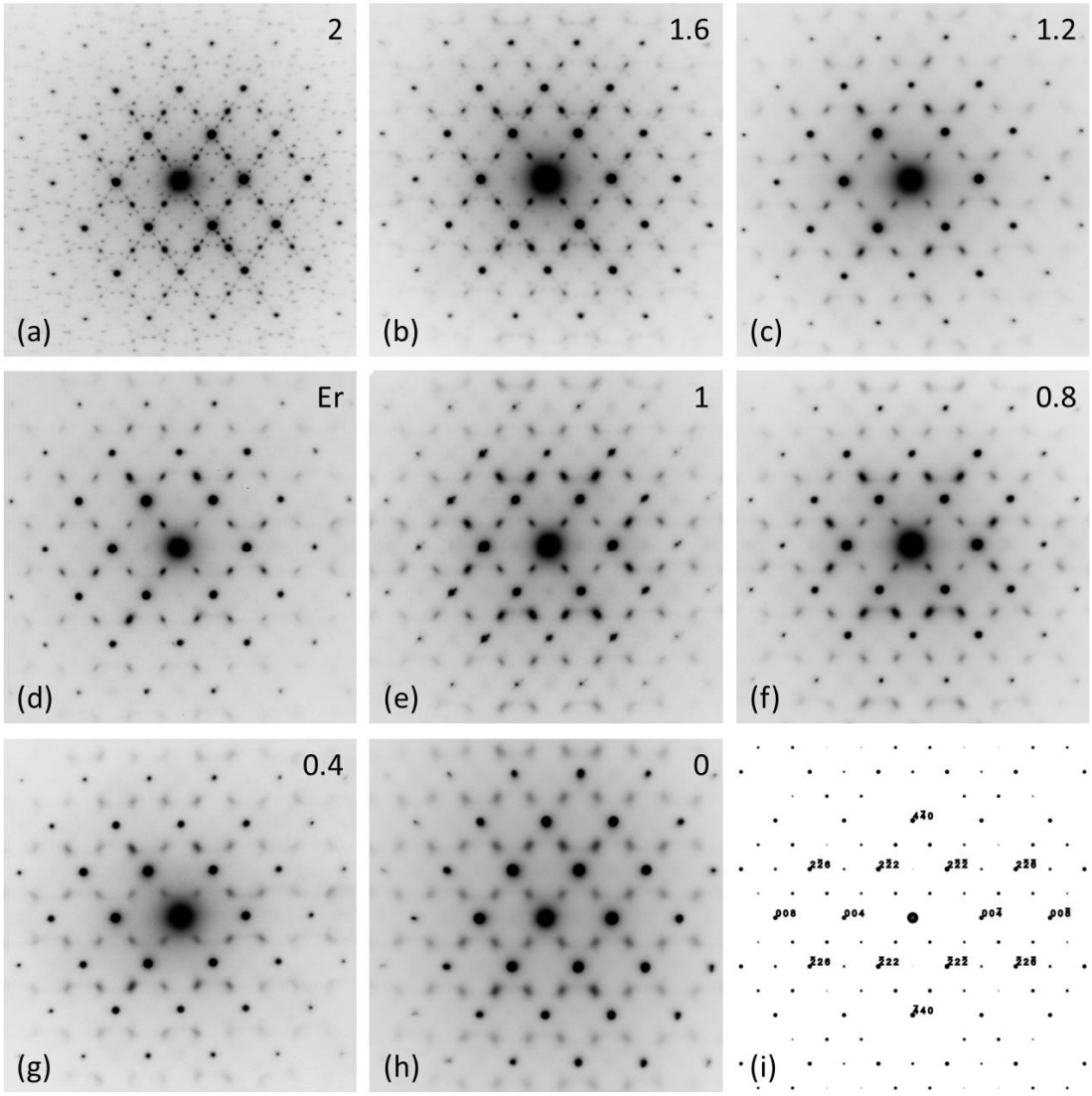

Figure 4. Selected area electron diffraction patterns for the $Ho_{(x)}Yb_{(2-x)}TiO_5$ series of compounds [(a) x = 2, (b) x = 1.6, (c) x = 1.2, (e) x = 1, (f) x = 0.8, (g) x = 0.4, (h) x = 0], (d) Er_2TiO_5, and (i) simulated (SingleCrystal software) pyrochlore (*Fd*$\bar{3}$*m* symmetry) diffraction pattern all viewed down zone axis [1 1 0].

Table 1.The Rietveld refined cell parameter, atomic positions, isothermal temperature factors (U_{iso}), and the statistics for goodness of fit between neutron powder diffraction data and calculated values.

Ho_2TiO_5, space group $Fd\bar{3}m$, a = 10.303(2)

Rp = 2.92 %, Rwp = 3.19 %, X^2 = 5.98

Element	x	y	z	U_{iso}*100	Occupancy
Ho (1)	0.5	0.5	0.5	2.1 (4)	0.813
Ti (1)	0.5	0.5	0.5	2.1 (4)	0.187
Ho (2)	0	0	0	10 (1)	0.524
Ti (2)	0	0	0	10 (1)	0.476
O (1)	0.375	0.375	0.375	2.8 (8)	1.00
O (2)	0.125	0.125	0.125		0
O (3)	0.3534(6)	0.125	0.125	10.5 (4)	0.946

Table 2. The cell parameters and statistics for goodness of fit for the $Ho_{(x)}Yb_{(2-x)}TiO_5$ series and Er_2TiO_5 compounds. *Yb_2TiO_5 data is from [16]. Ho_2TiO_5 and Yb_2TiO_5 are refinements from neutron powder diffraction data. All other data is from powder laboratory XRD (weighted Cu K-alpha).

	Ho_2TiO_5	**$Ho_{1.6}Yb_{0.4}TiO_5$**	**$Ho_{1.2}Yb_{0.8}TiO_5$**	**$HoYbTiO_5$**	**$Ho_{0.8}Yb_{1.2}TiO_5$**	**$Ho_{0.4}Yb_{1.6}TiO_5$**	***Yb_2TiO_5 [16]**	**Er_2TiO_5**
a	10.303(2)	5.13818(5)	5.12729(5)	5.12155(5)	5.11617(5)	5.10476(5)	5.09418(9)	5.1281(1)
R_{wp}	3.20%	5.48%	5.86%	4.71%	5.77%	5.81%	4.07%	6.66%,
X^2	6.03	4.69	5.13	3.21	5.01	5.61	2.21	5.18

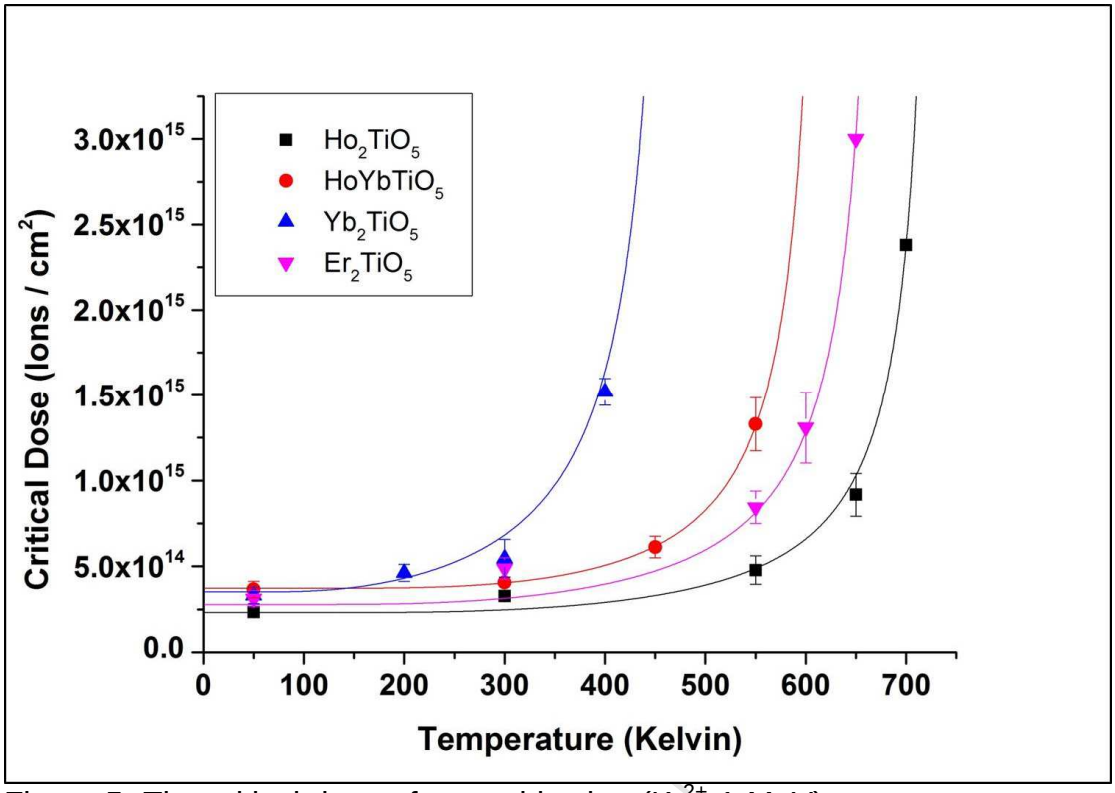

Figure 5. The critical dose of amorphisation (Kr^{2+} 1 MeV) versus temperature (Kelvin) plot of the $Ho_{(x)}Yb_{(2-x)}TiO_5$ series plus Er_2TiO_5. The lines of best fit, based on equation (1), were calculated and are fit to the data points.

Table 3. The calculated characteristics, from crystallographic data, plus ionic radius values compared with the calculated values from ion-irradiation response data for the $Ho_{(x)}Yb_{(2-x)}TiO_5$ series and Er_2TiO_5.
*Yb_2TiO_5 ion-irradiation data from previous study [40].

Compound	**Ln^{3+} (VIII) ionic radius (Å) [32]**	**Density (g / cm^3)**	**ENSP**	**D_{c0} (x10^{14}) Ions / cm^2**	**T_c (K)**
Ho_2TiO_5	1.015	7.46	0.602	2.32 (28)	738 (15)
$HoYbTiO_5$	1.00	7.65	0.627	3.73 (6)	628 (6)
*Yb_2TiO_5	0.985	7.93	0.653	3.52	479 (44)
Er_2TiO_5	1.004	7.61	0.645	3.27 (34)	689 (6)

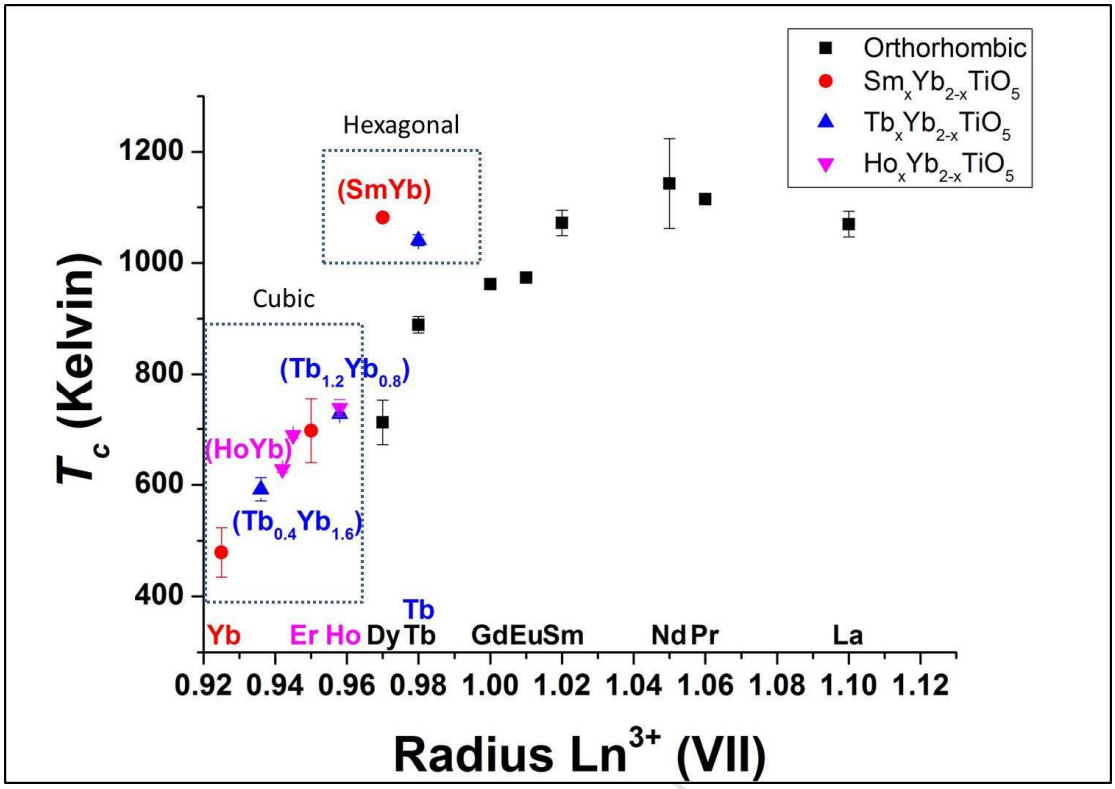

Figure 6. The ion-irradiation response, T_c, versus lanthanide radius for Ln_2TiO_5 compounds. Results are shown from this study ($Ho_{(x)}Yb_{(2-x)}TiO_5$) and are compared with results from previous studies; Ln_2TiO_5 with orthorhombic symmetry [5], $Sm_{(x)}Yb_{(2-x)}TiO_5$ with the four major symmetries [40], and $Tb_{(x)}Yb_{(2-x)}TiO_5$ with four major symmetries plus two polymorphs for Tb_2TiO_5 [41].

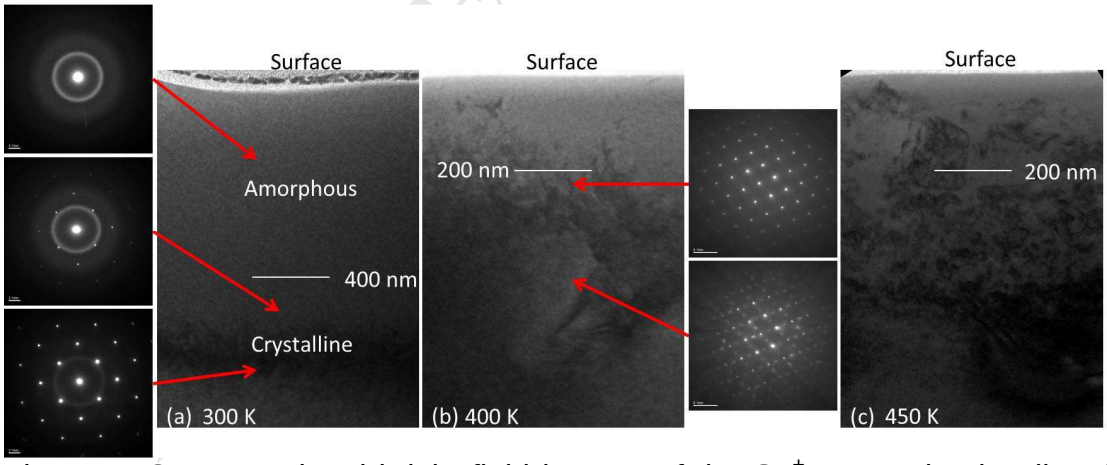

Figure 7. Cross-sectional bright field images of the Se^+ 1 MeV ion-irradiated Yb_2TiO_5 samples held at (a) room temperature (nano-diffraction showing various amounts of crystallinity with depth), (b) 400 K {nano-diffraction down zone axis [1 1 0] showing absence of pyrochlore reflection (1 1 1) in top NBD but presence in the below NBD}, and (c) 450 K. The images show a completely amorphous 400 nm deep section, indicated via homogeneous contrast, for the room temperature irradiation whilst samples held at higher temperatures tended to form domains of crystallinity throughout the irradiated depth.

Table 4. The calculated dpa for *in-situ* values are the average from the surface to 70 nm depth. The calculated dpa for *ex-situ* are based on the amorphous depth with the average taken from plus and minus 25 nm either side. The T_c value for *in-situ* is based on the calculation described in the methods section and for *ex-situ* is based on the temperature where crystallinity is detected within the surface to 200 nm volume.

Compound	$D_{c(300\ K)}$ *ex-situ* dpa	$D_{c(300\ K)}$ *in-situ* dpa	T_c (K) *ex-situ*	T_c (K) *in-situ*
Ho_2TiO_5	0.11	0.32	575 (25)	738 (15)
$HoYbTiO_5$	0.35	0.40	525 (25)	628 (6)
Yb_2TiO_5	0.79	0.55	425 (25)	479 (44)

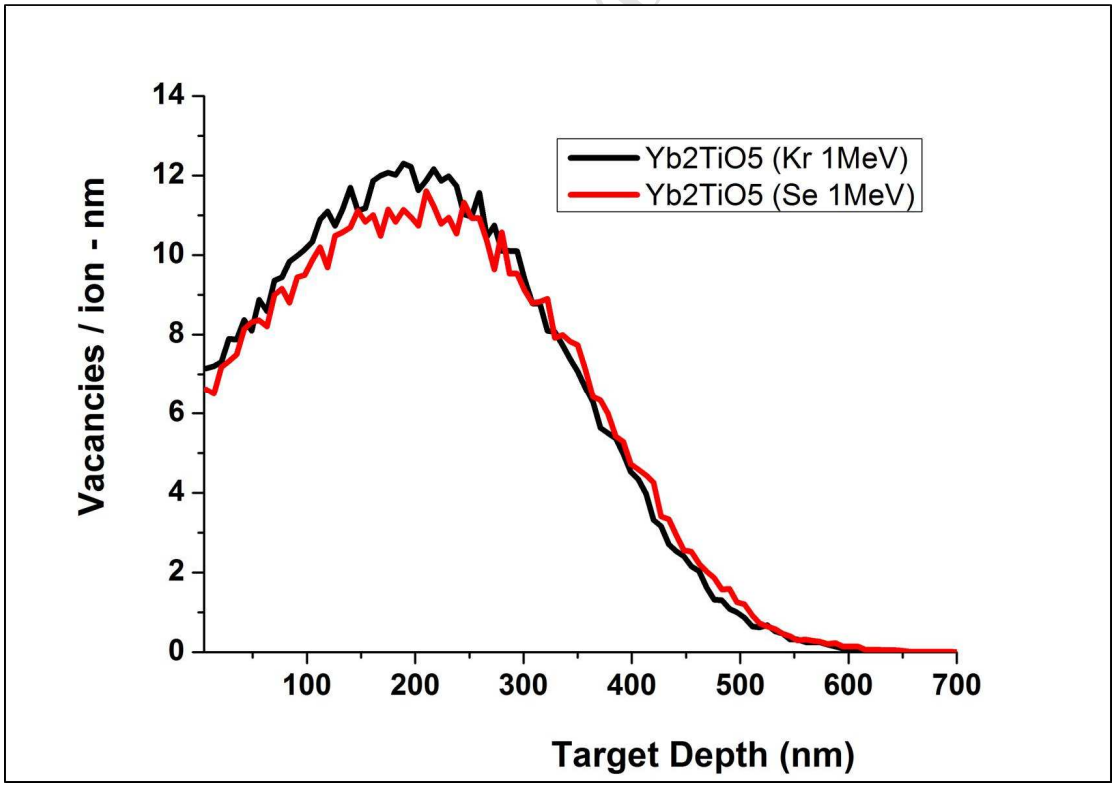

Figure 8. SRIM calculation based on NRT model, of the damage depth profiles comparing the response of Yb_2TiO_5 to ion-irradiation using 1 MeV Kr and 1 MeV Se.

Highlights
Journal of Nuclear Materials

The ion-irradiation tolerance of the pyrochlore to fluorite $Ho_{(x)}Yb_{(2-x)}TiO_5$ and Er_2TiO_5 compounds: a TEM comparative study using both *in-situ* and bulk *ex-situ* irradiation approaches.

- A systematic crystal structure refinement for the defect-pyrochlore to defect-fluorite $Ho_{(x)}Yb_{(2-x)}TiO_5$ and Er_2TiO_5 series of compounds is carried out.
- The *in-situ* (transmission electron microscopy) ion-irradiation tolerance for this cubic system is determined and trends discussed.
- A new *ex-situ* approach is used for quantifying ion-irradiation response and the results are compared with those of the *in-situ*.